



# Experimental and numerical investigations on novel post-tensioned precast beam-to-column energy-dissipating connections

Shuguang Wang <sup>a</sup>, Tianyang Zhang <sup>a</sup>, Weizhi Xu <sup>a,b,\*</sup>, Dongsheng Du <sup>a</sup>, Yunlong Zhang <sup>a</sup>

<sup>a</sup> College of Civil Engineering, Nanjing Tech University, Nanjing 211816, China

<sup>b</sup> Multi-Functional Shaking Tables Laboratory, Beijing University of Civil Engineering and Architecture, Beijing 102616, China

## ARTICLE INFO

### Keywords:

Unbonded post-tensioned prestress  
Hybrid connection  
Seismic behavior  
Energy-dissipating elements  
Numerical analysis

## ABSTRACT

This paper proposes novel self-centering post-tensioned hybrid connections (PTHC) with energy-dissipating elements, with assembly requiring grouting only once and convenient construction. To investigate the seismic performance of the hybrid connections, cast-in-place beam-to-column and assembled monolithic beam-to-column connection specimens were designed as comparison test specimens. Subsequently, four PTHC specimens with different test variables—restraint conditions of beam end, unbonded lengths of the energy-dissipating elements, energy-dissipating material, and initial prestress were designed and investigated by quasistatic experiments. The test results showed that the designed PTHC specimens had high energy dissipation capacity, good self-centering capacity, high ductility, and low accumulated damage. Concrete restraints at the beam end effectively restrained the buckling behavior of the energy-dissipating elements. Finally, numerical simulation models of the PTHC specimens were established to further investigate the effects of the design parameters on the bearing and energy dissipation capacity. Combined with the test results, the PTHC specimens were found to have good seismic resilience. Balancing the contributions of the energy-dissipating elements and prestress to the load carrying capacity appeared to be critical.

## 1. Introduction

Compared to traditional cast-in-place reinforced concrete structures, assembled concrete structures have the advantages of cost-effectiveness, accelerated construction speed, high standardization, and resource-saving [1–5]. In recent years, strengthening building industrialization and reinforcing urban resilience [6–8] have become inevitable trends in the construction industry. A self-centering precast concrete (SCPC) frame structure combines the two main advantages of assembly and functional restoration [9–11], which has generated varied interests. However, the seismic performance and integrity of prefabricated reinforced concrete (PC) structures are essentially governed by the properties of their beam-to-column connections [12], which emphasizes the importance of reliable and ductile connections to various prefabricated units. In contrast to conventional prefabricated beam-to-column connections, the beam and column units of SCPC connections are assembled by post-tensioned (PT) strands [13]. The intersections of the beams and columns in SCPC connections open up during an earthquake, and the PT strands provide recentering forces to the connections to restore the structural system to the state before the earthquake. Although an SCPC

system is characterized by low residual deformation and minor damage, its energy dissipation performance is poor. The prestressing of the PT strands squeezes the contact surfaces of the beams and columns, providing shear resistance, which causes significant deformation of the connections under a major earthquake and exposes new modes of damage.

The Precast Seismic Structural Systems (PRESSS) program first proposed the concept of SCPC frame connections and conducted a series of experiments [14]. In the fourth phase of the PRESSS program, Stanton et al. [15] significantly improved the energy dissipation performance of SCPC connections by placing energy-dissipating bars in the late grouting area [16].

In recent decades, an increasing number of energy-dissipating devices have been developed to improve the performance of SCPC connections. Morgen et al. [17,18] proposed a new type of friction damper for unbonded PT PC frame structures and established a fiber-spring model. The analytical results showed that friction-damped precast frames can achieve significant energy dissipation levels while maintaining high self-centering capability. Koshikawa [19] investigated the design of SCPC beam-to-column connections using friction devices, and

\* Corresponding author.

E-mail address: [xuwz@njtech.edu.cn](mailto:xuwz@njtech.edu.cn) (W. Xu).

proposed a design procedure to achieve desired moment and energy dissipation capacity. Moreover, Huang et al. [13] proposed variable-friction dampers for SCPC frames, and found that as the connection deformation changed, the friction force of the energy-dissipating device increased. The experimental results showed that the new type of beam-to-column joint achieved the expected energy dissipation performance and self-centering ability. In addition to friction-type energy-dissipating devices, other types of steel-yielding devices have been proposed for unbonded PT connections. Cai et al. [11] proposed a new type of self-centering beam-to-column connection with steel top and seat angles, and investigated eight specimens with three test variables: initial PT force, beam depth, and type of steel angles. The experimental results showed that the novel connection with a steel angle energy-dissipating device exhibited large initial stiffness, good recentering capacity, and high ductility. Wang et al. [9] developed a new SCPC beam-to-column connection with additional all-steel bamboo-shaped energy dissipators, and performed pseudo-dynamic tests on five specimens to investigate the effects of the novel dampers. The test results showed that the proposed connections exhibited stable hysteretic behavior and excellent self-centering capabilities. Li et al. [10,20,21] proposed a new type of low-damage SCPC frame connection with a replaceable mild steel damper, and a series of experiments showed that the seismic behavior of the novel SCPC frame was significantly enhanced. Although most external energy dissipators have stable energy dissipation capacity, their ineffective costs and inconvenient construction have gradually become weaknesses. Liu et al. [22] developed precast rocking concrete connections with miniature buckling-restraining braces, and achieved good self-centering ability.

In addition to the external energy dissipators used at beam-to-column surfaces [23], SPCP beam-to-column connections using pre-stressing tendons and embedded unbonded bars have been extensively studied [24]. Ozden and Ertas [25] investigated the effect of different mild steel reinforcement contents on the structural performance of PT precast connections, suggesting that 20%–30% mild steel reinforcement contribution to the flexural strength is rational. Song et al. [26] introduced SCPC frames using hybrid joints to connect all precast elements, developed analysis models in OpenSees, and proposed empirical equations to quantify the distribution of the hysteretic energy demand in hybrid joint-based self-centering structures. Wang et al. [27–29] developed replaceable slip-free steel bars to provide SCPC beam-to-column connections with high energy dissipation capacity, and the novel connections exhibited superior resilience to conventional cast-in-place connections. However, the ultimate distribution of cracks at a 1/18 drift ratio was reasonably widespread, and when a specimen was unloaded, the cracks extended to the middle of the beam, instead of at the beam end. Li et al. [30] developed a novel precast prestressed concrete frame with nonprestressed grouted steel bars, and cyclic loading experiments and numerical simulations showed that the frame achieved satisfactory seismic performance.

Compared to external energy dissipators, embedded unbonded energy-dissipating bars in connections have the following advantages: simpler construct design, more space-saving, lower residual deformation, and higher energy dissipation efficiency. In this study, novel PT hybrid connections (PTHCs) were developed that can overcome the drawbacks of external energy-dissipating connections. In contrast to existing self-centering hybrid connections [25–29], the energy-dissipating bars of the PTHC specimens were prefabricated in the columns when a short grouting groove was reserved for the precast beams. Moreover, grouting was required only once during connection assembly. The moment bearing capacity of the PTHC specimens was jointly determined by the embedded unbonded energy-dissipating bars and the PT strands. As the deformation of the connections increased, the energy-dissipating elements entered a state of significant yielding [31], which is shown in Fig. 1. Based on the mechanical characteristics of the unbonded energy-dissipating bars in the PTHC specimens, a series of cyclic load tests were conducted on four hybrid connections. The following

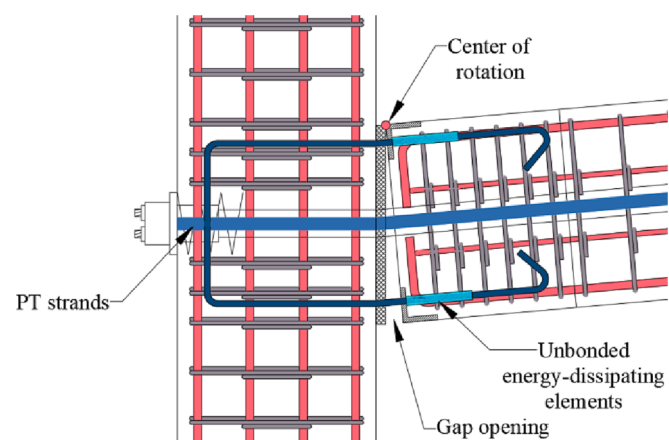


Fig. 1. Deformation of PTHC in yield limit state.

parameters were investigated: geometric and material properties of the unbonded bars, PT force, and reinforced measures for the beam end. Furthermore, a cast-in-place beam-to-column connection (CBCC) and an assembled monolithic beam-to-column connection (AMBC) were formed as contrast specimens. The crack development, component damage, seismic behavior, prestressing forces, and strains of the critical parts of the connections were examined by low-cycle reciprocating experiments. Based on the tests, a detailed finite element (FE) model was established to further investigate the effects of the design parameters on the hysteresis behavior and failure modes of the beam-to-column connections.

## 2. Experimental program

### 2.1. Specimen description

To study the damage mechanisms and seismic performance of the novel hybrid connections and observe the damage patterns of their PC components and energy-dissipating bars, four full-size PTHC specimens were designed. Rectangular slotted holes were reserved at the precast beam-end for pouring grout to anchor the energy dissipating elements. The energy-dissipating bars were partially unbonded prior to assembly by wrapping the energy-dissipating elements with unbonding materials. After the beam and column had been assembled, a concrete bedding layer needed to be poured at the junction and then tensioned for pre-stressing, as shown in Fig. 2. The designs were based on the following parameters: unbonded lengths, diameter, and material of the energy-dissipating elements and the prestressing magnitude. In addition, CBCC and AMBC specimens were designed as comparison test specimens.

The cross-sectional dimensions of the columns for all specimens were 400 mm × 400 mm, the height was 2846 mm, the beam section was 250 mm × 400 mm, and the length was 2075 mm. The longitudinal reinforcement ratios of the columns and beams of the six specimens were 1.51% and 0.60%, respectively, and the details of the reinforcements for all specimens are illustrated in Fig. 3.

The calculated yield moment at the beam end of the CBCC as a reference specimen was 79.10 kN·m, and the yield moment of other specimens were equivalent to that of the CBCC. In the AMBC specimen, sleeves were used to connect the prefabricated beam and the upper and lower PC columns to achieve an equivalent effect to a cast-in-place connection. The reinforcement information was the same for all four hybrid connections. The contributions of the PT strands and the unbonded energy-dissipating elements to the yielding moment capacity were 60% and 40%, respectively, using the calculation method proposed by Song et al. [32]. The initial prestress was 276.3 kN, and the yield strength of the single-sided energy-dissipating elements was 94 kN. The energy-dissipating bars of PTHC-1—PTHC-3 with diameters of 12 mm

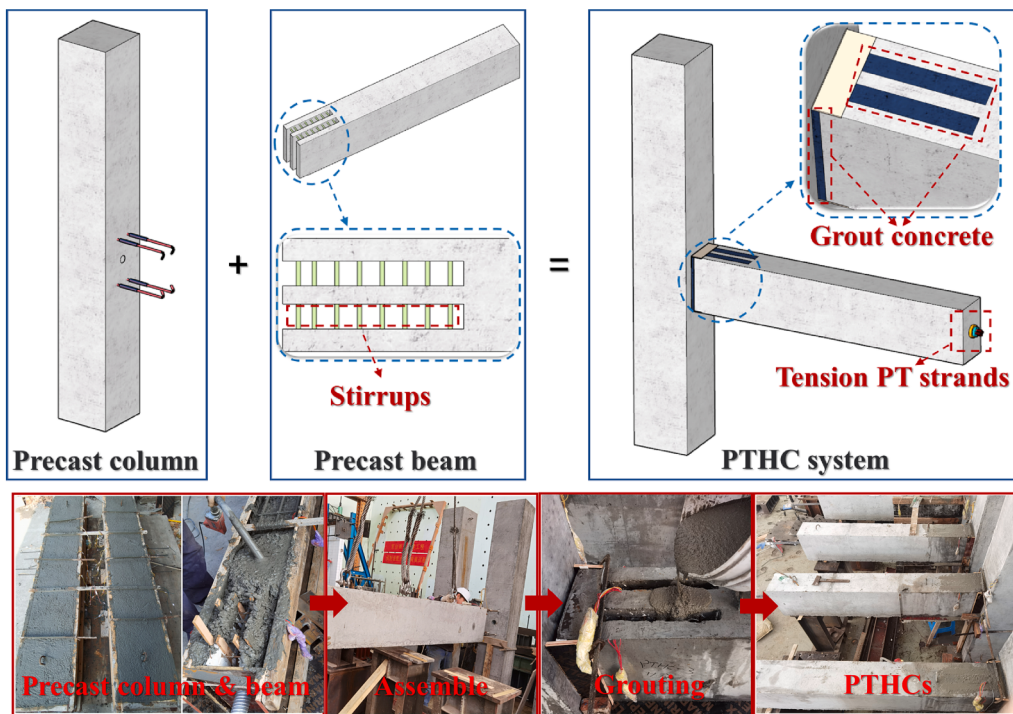


Fig. 2. Schematic diagram of the PTHC specimens.

had a nominal yield strength of 400 MPa (HRB400 steel bar in Chinese code [33]), which was used to calculate the reinforcement area. PTHC-4 had built-in unbonded strips (cross-sections of  $30 \text{ mm} \times 10 \text{ mm}$ ) with a nominal yield strength of 160 MPa, which was equivalent to the contribution of the energy-dissipating bars to the bending moment at the beam end. Detailed information on the specimens is provided in Table 1. The length-to-diameter ratio ( $L / D$ ) has a significant effect on the nonlinear mechanical behavior of energy-dissipating elements [34]. The energy dissipation of the energy-dissipation elements was lower at  $L / D = 10$  compared to  $L / D = 5$ , but the fatigue performance was better. When  $L / D \leq 6$ , the mechanical properties of the energy-dissipating elements were close, therefore the unbonded lengths of 60 mm and 120 mm were chosen.

The prestressing strands used in the PTHC specimens consisted of four wire strands, each with a nominal diameter of 15.2 mm and an area of  $140 \text{ mm}^2$ , for a total prestressing area of  $560 \text{ mm}^2$ . The initial prestress setting was 281 kN for all specimens, except PTHC-3, for which the initial prestress was 468 kN.

The design parameters of the built-in unbonded energy-dissipating elements are listed in Table 1. The unbonded elements of the PTHC specimens were prebuilt in their columns. Among them, the energy-dissipating bars of PTHC-1–PTHC-3 were U-shaped, and the energy-dissipating strip of PTHC-4 was reinforced with pins at the end, which can be seen in Fig. 2(c) and (d). The unbonded length of PTHC-1 was 60 mm, whereas those of the other specimens were 120 mm. In order to strengthen the restraining effect on the concrete at the beam ends of specimens PTHC-3 and PTHC-4, angle steel with a nominal yield strength of 345 MPa, type L80 × 5, were used and installed on the top and bottom surfaces of the beams, and steel bar with diameter of 8 mm and nominal yield strength of 335 MPa was used to weld and fix the Angle steel at the upper and lower ends. After the angles were installed and positioned, the beam ends were grouted with concrete and the connecting rebars for the angles was buried in the grout together.

## 2.2. Material properties

The mechanical properties of the materials used in all connections

are listed in Table 2. The average yield strength of the longitudinal stress reinforcement for all specimens was 437 MPa, the ratio of tensile strength to yield point is 1.46 and an elongation at fracture of 20.84%. The ultimate strength of the PT strands was 1857 MPa, and the yield strength values of the unbonded HRB 400 steel and unbonded mild steel materials of the built-in energy-dissipating elements were 554 MPa and 180 MPa, respectively. Concrete compressive material experiments were conducted according to the Standard Chinese Code (GB/T50107-2010) [35], and the 28-day strength of concrete was above 40 MPa for all specimens, with the highest strength for the CBCC.

## 2.3. Test setup

The arrangement of the loading device and sensors is shown in Fig. 4. The loading point at the top end of the column of a specimen was connected to an MTS actuator through holding rods. The column was hinge-supported at the bottom and laterally restrained at the top by rollers, which acted as the upper and lower contra-flexural points of the column respectively. The beam end was also connected to a ground anchor using an articulated link to achieve a hinge-supported boundary restraint. The axial pressure of the column was achieved by tensioning with four 600 kN jacks. During the experiments, axial pressure ratio of 0.3 was chosen to determine the vertical axial force of 916.80 kN. An initial prestress was applied prior to the horizontal loading of the PTHC specimens, and a 500 kN core piercing jack was installed at the beam end for tensioning the prestress. In addition, a force transducer with a range of 1000 kN was placed between the column sides to monitor whether the prestress was applied to a predetermined value and measure the change in the prestress during the entire loading.

Ten Linear variable displacement transducers (LVDTs) were arranged to measure the deformation of the specimens at different positions. LVDTs-1 and -3 were used to measure the angles of rotation between the beams and columns of the CBCC and the AMBC as well as the opening angles of the PTHC specimens. LVDTs-2 and -4 were primarily designed to monitor the occurrence of plastic deformation at measured positions. LVDTs-7 and -8 measured the vertical and horizontal displacements of the beam end, respectively. LVDTs-9 and -10

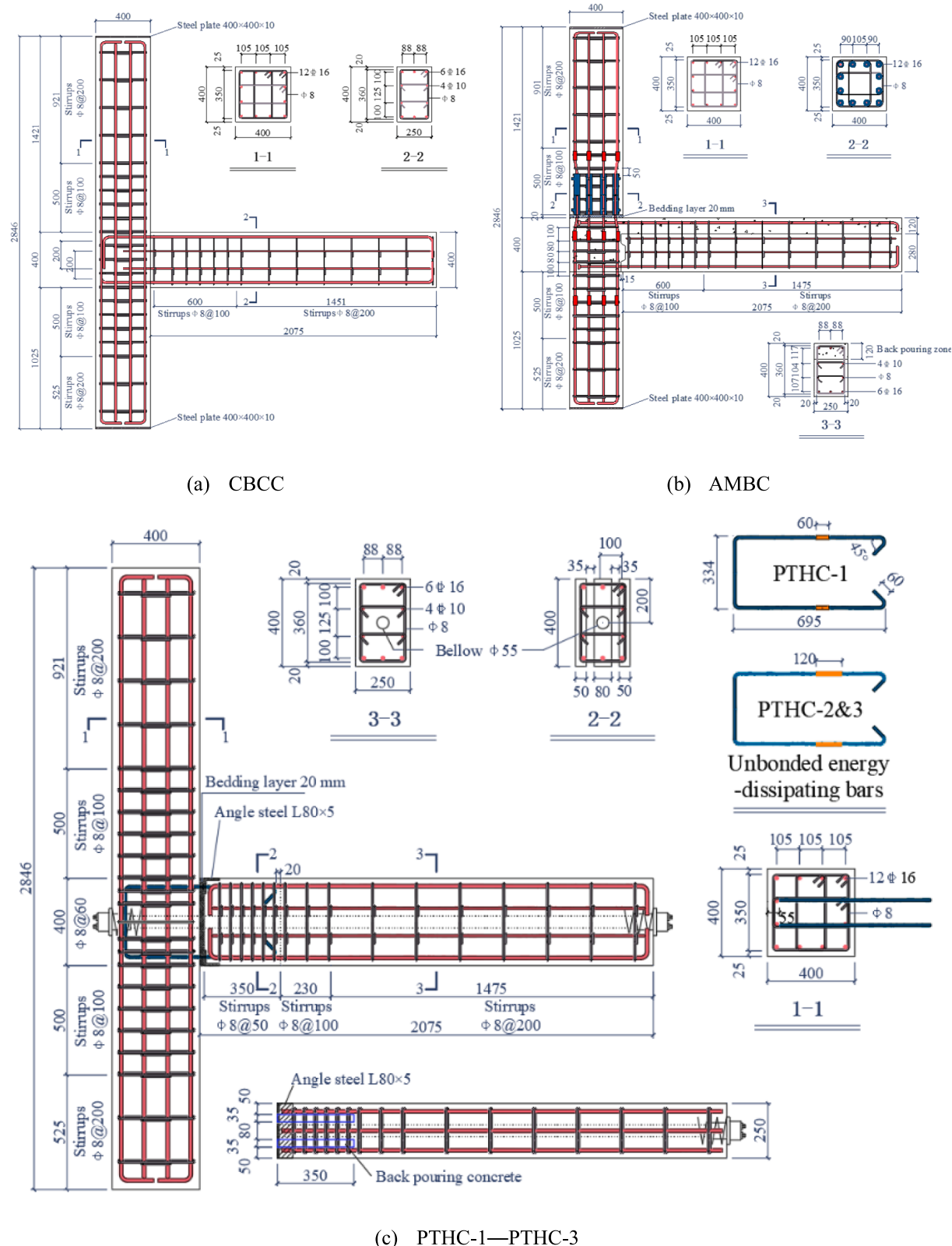


**Fig. 3.** Geometry and reinforcement details of all PTHC connections.

were used to measure the slip between the column and the base to correct the actual loading displacement.

As shown in Fig. 5, a series of strain gauges are used to measure the axial strains of the reinforcements and the unbonded energy-dissipating

components. The naming scheme of the strain gauges begins with a letter followed by a number (where B, C, and U denote a beam, a column, and an unbonded energy-dissipating component, respectively).

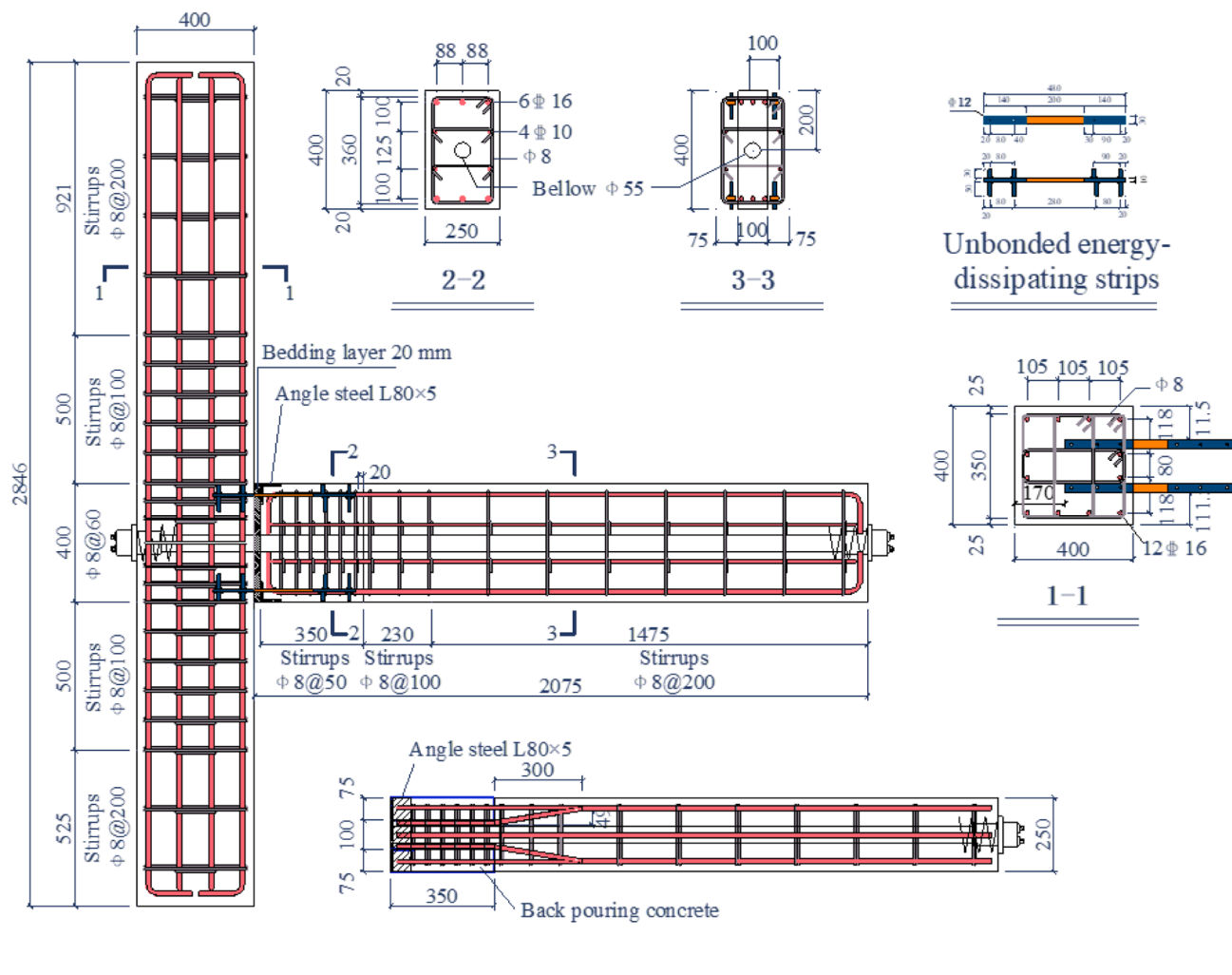


Fig. 3. (continued).

**Table 1**  
Description of specimens.

Specimen	Designed initial PT force (kN)	Energy-dissipating elements	Unbonded length (mm)
CBCC	/	/	/
AMBC	/	/	/
PTHC-1	281	HRB400 steel	60
PTHC-2	281	HRB400 steel	120
PTHC-3	468	HRB400 steel	120
PTHC-4	281	Mild steel	120

#### 2.4. Loading protocol

Two types of variable displacement amplitude (VDA) loading schemes were used in the experiments. The first loading mode, VDA-1, was variable-amplitude loading. Specifically, before the formal loading, a cycle with a displacement amplitude of 2 mm was conducted to check whether the various test acquisition systems were working normally. Subsequently, loading was applied for three cycles, and the connection rotations of each stage were 0.2%, 0.25%, 0.35%, 0.5%, 0.75%, 1%, 1.5%, 2%, 2.75%, and 3.5%. In the actual loading process, if the bearing capacity did not significantly decrease after loading to a rotation of 3.5%, drifts of 4.25% and 5% were added successively until the bearing capacity decreased by more than 20%. This is shown in

Fig. 6(a).

The second loading scheme VDA-2, as shown in Fig. 6(b), was used to investigate the low-cycle fatigue properties of the PTHC specimens. As the maximum inter-story drift ratio limit for concrete frame structures under rare earthquakes as specified in the Chinese Code [36], an inter-story drift ratio of 2% was applied in reciprocal loading. If the load capacity of the connection did not decrease by more than 15% after 30 cycles of loading [37], the loading was continued by increasing the drift amplitude.

### 3. Experimental results and discussions

#### 3.1. Failure modes and crack distributions

The cracking developments of the specimens at different drift ratios are shown in Fig. 7, in which the cracks are marked in black and red. The consolidated results of the failure phenomena of all specimens are summarized in Table 3.

The damage patterns of the CBCC and AMBC are similar, with cracks concentrated at the beam ends and no remarkable damage in the column and connection areas, as shown in Fig. 7(a) and (b). In the CBCC specimen, the first crack developed under loading at a drift of 0.2%, and it was approximately 150 mm from the beam end. Subsequently, additional cracks became concentrated within 400 mm of the beam end, in the drift range of 0.5%–3.5%. Wide non-closable cracks appeared when

**Table 2**  
Material properties.

Reinforcement bars and PT strands			Unbonded energy-dissipating bars			Concrete		
Diameter (mm)	$f_y$ (MPa)	$f_u$ (MPa)	Type	$f_y$ (MPa)	$f_u$ (MPa)	Specimen	14-day strength (MPa)	28-day strength (MPa)
16 (Bars)	437	637	HRB400 steel	554	634	CBCC	46.30	48.51
15.2 (PT strands)	1720	1857	Mild steel	180	280	AMBC	30.60	42.12
						PTHC-1	35.28	41.22
						PTHC-2	35.28	41.22
						PTHC-3	35.57	45.75
						PTHC-4	35.20	46.55

the drift reached 3.5%. As the drift continued to increase, the protective layer of concrete spalled off at the beam end, eventually forming a concrete spalling zone approximately 500 mm in length, and caused the longitudinal reinforcement of the beam to considerably bend. In the AMBC specimen, the first crack was closer to the beam end than in the CBCC specimen, and the damage distributed on the upper and lower sides of the beam was noticeably asymmetrical. The degree of concrete damage to the AMBC was significantly higher than those of the cast-in-place connections, and the length of the plastic hinge zone at the beam end was approximately 200 mm.

The PTHC-1 and PTHC-2 specimens differed in design details, except for the unbonded lengths of the energy-dissipating elements. When PTHC-1 was loaded to a drift of 0.35%, the first crack appeared on the upper side of the beam, approximately 410 mm away from the beam end, and the crack length was approximately 50 mm. Before the drift reached 3.5%, the PC beam of PTHC-1 exhibited almost no damage, and the deformation was concentrated in the beam–column interface area. However, when the specimen reached a 3.5% drift, considerable horizontal cracks appeared on the lower side of the beam end and the upper side was severely crushed. The concrete spalled extensively within 200 mm of the beam end, and the energy-dissipating bars exhibited significant compression buckling fractures in the unbonded section. The above phenomena are shown in Fig. 7(c). The first crack in the PTHC-2 specimen appeared at a drift of 0.5%; it was approximately 80 mm in length and was located at a similar position to that in PTHC-1. The main parts of the components remained elastic until a drift of 2%. The final failure pattern of PTHC-2 was similar to that of PTHC-1, with diffuse cracking at the upper part of the beam end and little damage to the lower side. The unbonded part of the energy-dissipating bars was exposed, flexed, and arched upward, which can be seen in Fig. 7(d).

PTHC-3 was designed to investigate the low-cycle fatigue performance of the hybrid connections, and the loading cycle was concentrated at a drift of 2%. Restraint measures were used to protect the concrete at the beam end, and the remainder of the construction details were the same as those of PTHC-2. The first crack in PTHC-3 also appeared at a drift of 0.5% and was approximately 40 mm in length. When the drift was first loaded in the negative direction to 3.5%, the unbonded bars pulled out and the load capacity decreased simultaneously. No cracks were observed in the column, particularly in the beam-to-column connection panel region, throughout the loading history; however, a part of the concrete bedding was broken. The above phenomena are shown in Fig. 7(e).

The PTHC-4 post-grouting locations were on both sides of the PC beam, and the energy-dissipating material was mild steel. The crack development and the damage pattern are shown in Fig. 7(f). The first crack occurred at a 0.5% drift at the interface of the grout layer and the column, approximately 250 mm from the beam end, and a vertical crack with a length of approximately 50 mm appeared on the upper and lower sides. After loading to a drift of 4.25%, the unbonded mild steel fractured. Owing to the effective restraint of the beam-end concrete, the

specimen was only partially damaged at the bedding layer and could be repaired to restore its original function.

### 3.2. Load–drift hysteresis curve

The hysteresis curves for each connection are shown in Fig. 8. Feng et al. [38] proposed the farthest point method to determine the yielding point of a skeleton curve without remarkable turning, which was used to determine the yield points of the test specimens in this study.

As monolithic specimens, both the CBCC and AMBC did not show remarkable pinch-shrinkage characteristics in the hysteresis curves, which presented a “spindle shape” in general, reflecting their strong energy dissipation capacity with a “strong column–weak beam” configuration. Both the CBCC and AMBC were ductile connections; therefore, their skeleton curves were close to the “double broken line,” in Fig. 8(a) and (b). At large drifts, a considerable fall was caused in the skeleton curves by the concrete cracking and the compression buckling of the reinforcements. The yield force and maximum load capacity of the AMBC were lower than those of the CBCC, and the envelope area of the hysteresis curve was considerably smaller, which indicates that the integrity of the former was weaker than that of the latter.

The PTHC-1–PTHC-4 specimens presented flag-shaped hysteresis owing to the self-resetting effect of the PT strands. When the same prestress was applied to PTHC-1 and PTHC-2, no remarkable difference was observed in the shapes of their hysteresis curves, as shown in Fig. 8(c) and (d). When the drift reached 3.5%, the connection strength was considerably degraded by the insufficient constraint of concrete on the energy-dissipating bars.

As the prestress increased, the curve of PTHC-3 became more pinched, as shown in Fig. 8(e). After 30 cycles of loading at a 2% drift, when the amplitude increased to 2.75%, the strength of the connection considerably degraded and subsequently increased at the last loading level. Due to the error of the test operation, after 30 cycles of low-cycle fatigue loading, the PT strands locally fractured, resulting in an abrupt loss of the prestress and an abnormal decline in the bearing capacity. For the same energy-dissipating areas of the unbonded bars, the yield and maximum strengths of PTHC-3 were significantly improved compared to those of PTHC-2 on increasing the prestressing. Owing to the effective restriction of the concrete at the beam end, the strength degradation of PTHC-3 was better than those of the first two connections.

The material of the energy-dissipating strips embedded into PTHC-4 was mild steel, which had a low yield point and good ductility. Owing to the considerably more strain hardening of mild steel than that of ordinary reinforcing steel, the skeleton curve of PTHC-4 showed that its stiffness after yielding was significantly higher than those of the other specimens. At a 4.25% drift, because the energy-dissipating strips undergo considerable tensile deformation, the strips on the upper side of the beam were pulled off, and the load capacity of PTHC-4 was reduced, as shown in Fig. 7(f).

A comparison of the envelope curves of the six specimens is shown in

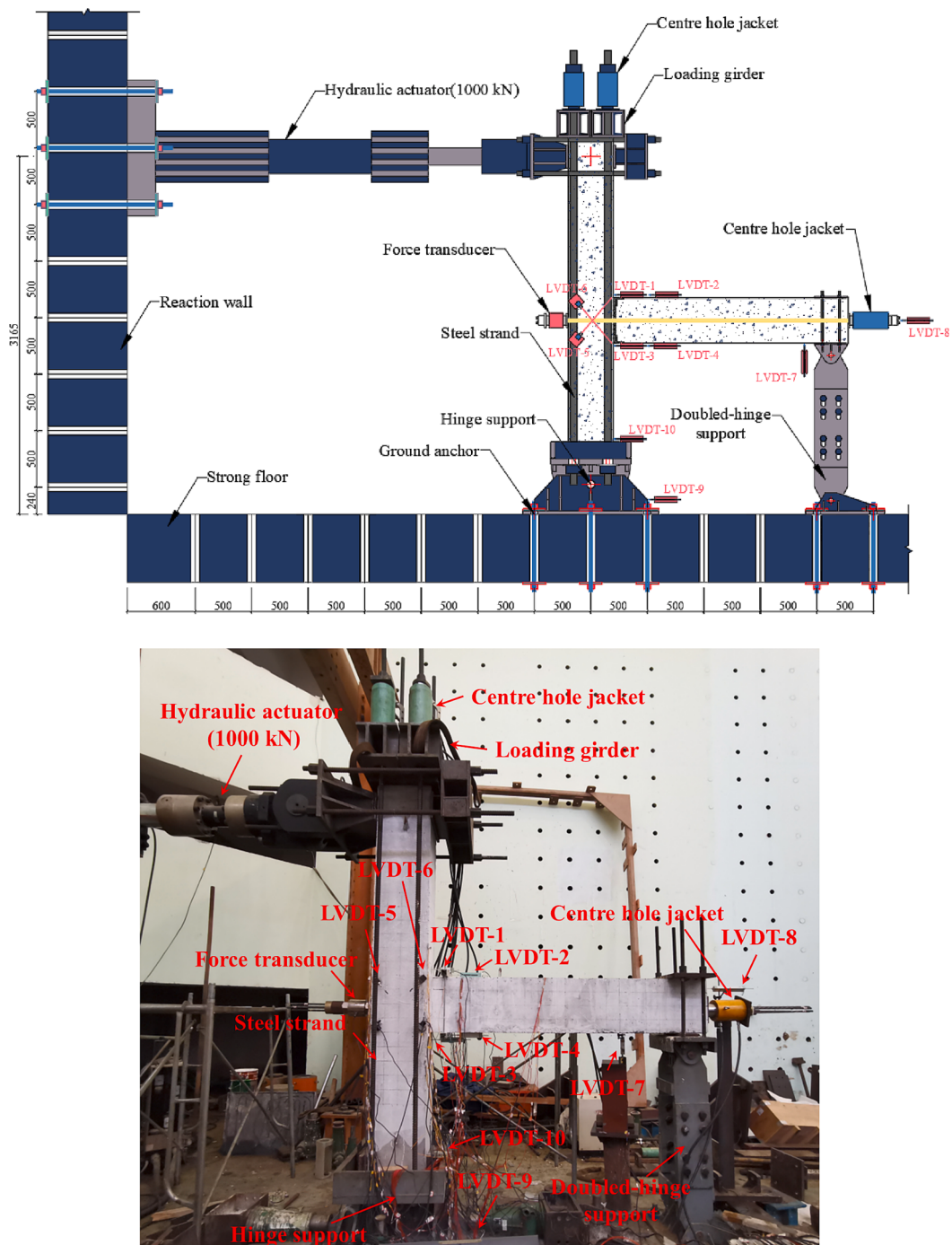


Fig. 4. Test setup.

**Fig. 9.** The bearing capacity of PTHC-3 was relatively high, which indicated that increasing the prestress can significantly improve the bearing capacity of the PTHC specimens. PTHC-4 had better energy dissipation and ductility owing to the use of low-yield-point steel; however, its residual deformation was higher. Overall, the bearing capacity of the PTHC specimens was comparable to that of the CBCC because of the suitable prestressing and energy-dissipating materials after reasonable restraint of the beam end.

### 3.3. Behaviors of PT forces

The prestress–drift relationships of the PTHC-1–PTHC-4 specimens are shown in Fig. 10. When the drift was below 0.25%, no significant

change was observed in the prestress of each specimen. As the drift ratio increased, the opening of the gap at the beam–column interface gradually expanded, and the prestress was increased by the tensile deformation of the PT strands. PTHC-1 and PTHC-2, without effective restraint reinforcement of the concrete at the beam ends, presented a considerable decrease in their prestresses with increasing deformation when the drift ratio reached 2.75%, as shown in Fig. 10(a) and (b). The beam end of PTHC-2 was subjected to multidirectional stresses under reciprocating loads and the concrete gradually diffused and cracked. So that the beam-end dropped and the actual center of rotation of the connection shifted downwards and the actual tensile length of the PT strands was subsequently reduced in the positive direction of loading, the curve is therefore asymmetrical from positive to negative. The initial prestress of

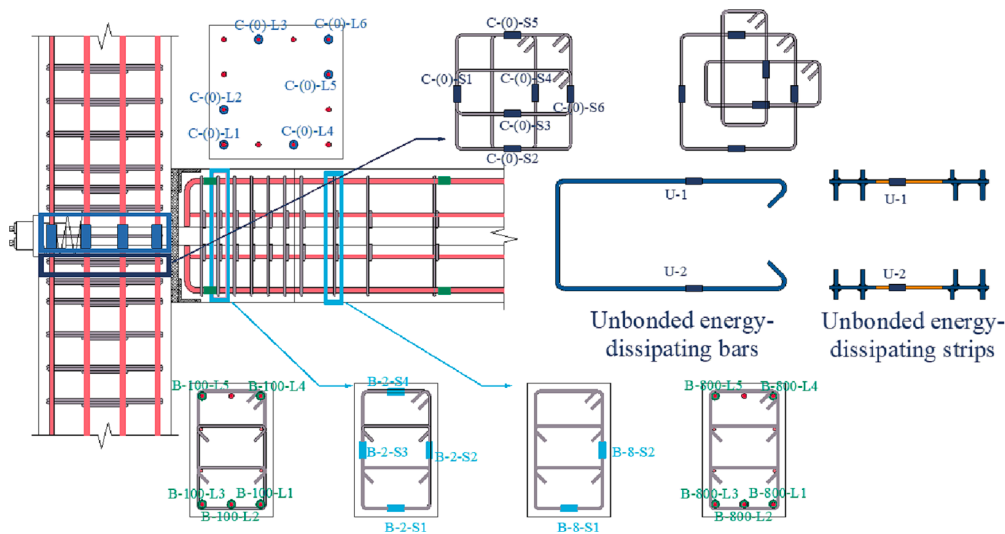


Fig. 5. Strain gauges for experiments.

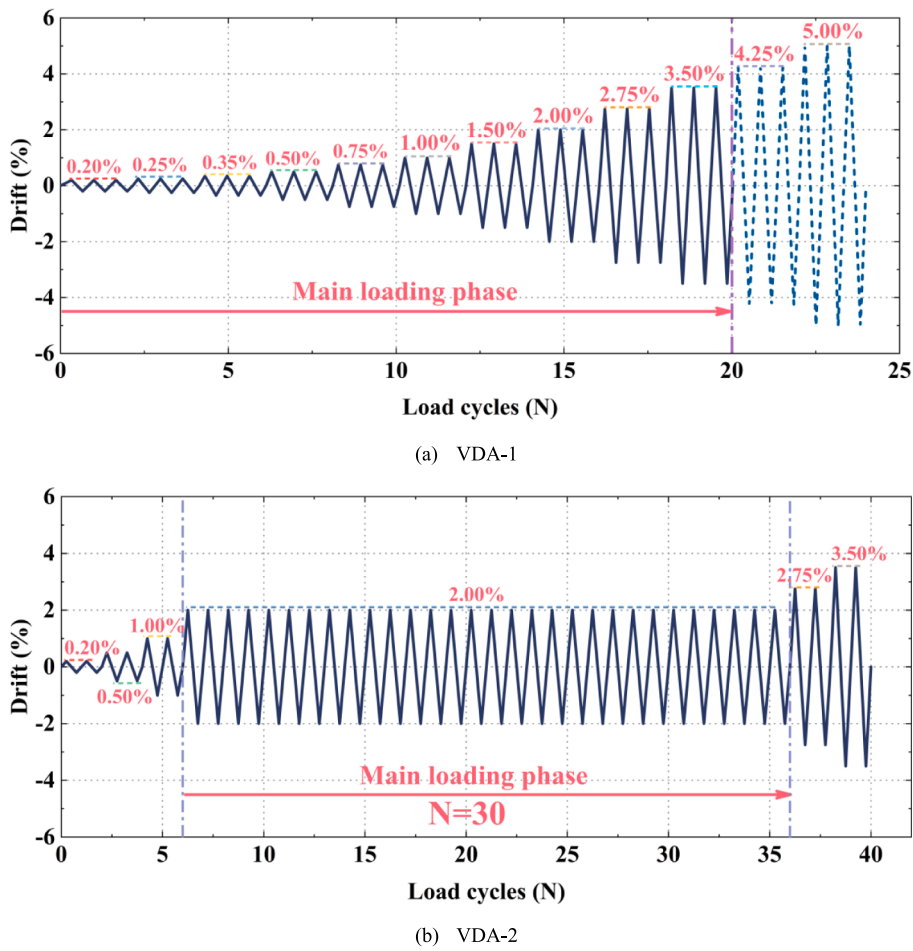


Fig. 6. Loading protocols of experiments.

PTHC-3 was higher than those of the other three hybrid connections. The damage of the PT strands caused the prestress to abruptly decrease when the drift was 2.75%, followed by which the prestress tended to increase. These results indicated that confined beam-end concrete was beneficial for the full exploitation of the mechanical properties of PT strands, as shown in Fig. 10(c). The initial prestress of PTHC-4 was

closest to that of PTHC-1, whereas the loss rate of the prestress was 12.32% lower than that of PTHC-1, which also indicated less damage to the component in PTHC-4, as shown in Fig. 10(d).

The maximum prestress during the loading history of each hybrid connection was 565.70 kN, which was 54% of the ultimate tensile strength of the PT strands, indicating that the PT strands of all specimens

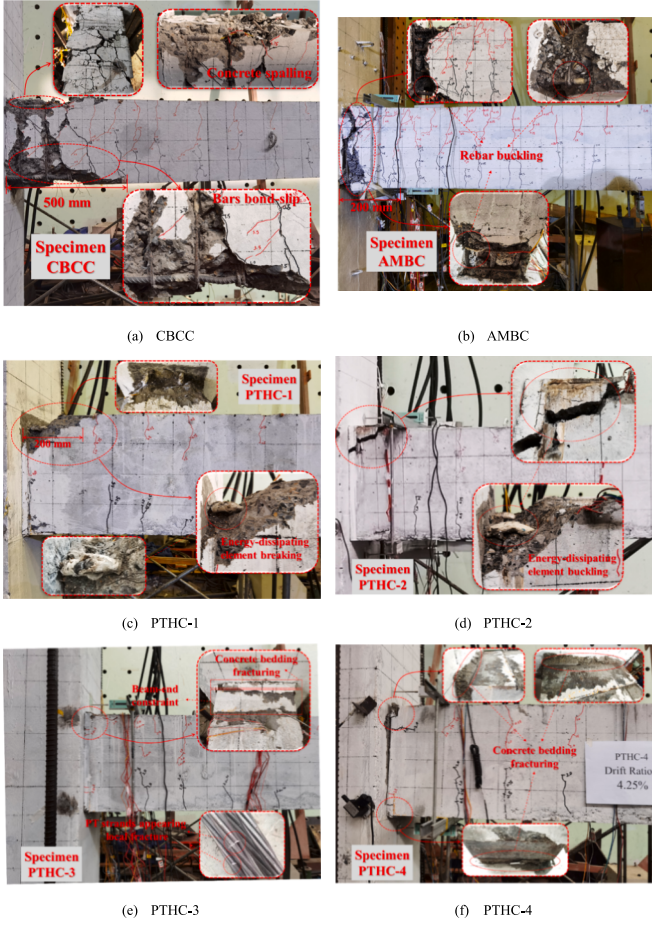


Fig. 7. Failure modes of all specimens.

**Table 3**  
Summary of experimental phenomena.

Specimens	Length of plastic zone (mm)	Damage state of beam-end
CBCC	500	Obvious plastic hinge, Concrete cracking, Rebar buckling
AMBC	200	Obvious plastic hinge, Concrete cracking, Rebar buckling
PTHC-1	200	Concrete cracking, Energy-dissipating elements cracking
PTHC-2	150	Concrete cracking, Energy-dissipating elements cracking
PTHC-3	< 100	Energy-dissipating elements cracking
PTHC-4	< 100	Energy-dissipating elements cracking

were elastic throughout the loading process. The prestress loss rates of these four connections range from 6% to 10%, with the highest prestress growth rate of 47.24% for PTHC-4.

#### 3.4. Stiffness degradation

Stiffness degradation is an important dynamic property of a structural component, and is influenced by crack development, yielding of the reinforcement, and plastic damage to the concrete [39]. The secant stiffness values obtained from the hysteresis curves of the specimens were used to evaluate their stiffness degradation. Stiffness degradation [40] is expressed as follows:

$$K_{\text{seci}} = \frac{(|+F_{\max i}| + |-F_{\max i}|)}{(|+\theta_{\max i}| + |-\theta_{\max i}|)} \quad (1)$$

where  $+F_{\max i}$  and  $-F_{\max i}$  are the peak strengths of the  $i$ th positive and negative peak points, respectively, and  $+\theta_{\max i}$  and  $-\theta_{\max i}$  are the relative displacements of the  $i$ th positive and negative peak points, respectively (see Fig. 11(a)).

The stiffness degeneration-drift curves of the connections are shown in Fig. 11(b). The initial stiffness values of the CBCC and AMBC were very similar to each other; however, as the drift ratio increased, the stiffness degradation of the AMBC occurred at a higher rate. The cut-line stiffness of the AMBC was lower than that of the CBCC, which was consistent with the experimental phenomenon. As the AMBC entered the nonlinear stage, it exhibited poor structural integrity and low stiffness. The overall stiffness values of the PTHC specimens were higher than those of the monolithic connections in the early stage. Among all hybrid connections, PTHC-3 exhibited a gentle stiffness degradation, which demonstrated that the prestressed force considerably contributed to the stiffness of the connections.

#### 3.5. Energy dissipation capacity

The equivalent viscous damping ratio  $\xi_e$ , was used to study the energy dissipation capacity of connections in the entire drift ratio range [41], and it was calculated using Eqs. (2) and (3).

$$\xi_{ei} = \frac{E_{Hi}}{2\pi \cdot K_{\text{seci}} \cdot \theta_{\max i}} \quad (2)$$

$$\theta_{\max i} = \frac{|+\theta_{\max i}| + |-\theta_{\max i}|}{2} \quad (3)$$

where  $E_{Hi}$  denotes the envelope area of each hysteretic loop as shown in Fig. 11.

The equivalent viscous damping ratios of all the specimens exhibited similar trends, in that the ratio first decreased and subsequently increased at a small drift, owing to the residual deformation affecting the hysteresis curve envelope area. The maximum equivalent viscous damping ratios of the six specimens during the loading history were 29.38%, 31.08%, 19.61%, 17.82%, 14.80%, and 24.32%, as shown in Fig. 12. Compared to the other connections, the AMBC had a higher damping ratio because its concrete was considerably crushed at the beam end, and consequently, some longitudinal reinforcements were unbonded and dissipated energy. PTHC-1 had a higher equivalent viscous damping ratio than PTHC-2, which indicated that the small lengths of the unbonded bars considerably increased the energy dissipation capability. However, as the prestressed force increased, the damping ratio of PTHC-3 remained at a relatively low level, which suggested that the initial prestress force had no effect on the energy dissipation capability of the PTHC specimens. Owing to the beneficial properties of mild steel, PTHC-4 outperformed the other three hybrid connections in terms of energy consumption throughout the loading process.

#### 3.6. Self-centering capability

The self-centering capabilities of all connections were evaluated using the relative self-centering ratio (RSCR), as follows:

$$RSCR_i = 1 - \frac{|+\theta_{\text{resi}}| + |-\theta_{\text{resi}}|}{|+\theta_{\max i}| + |-\theta_{\max i}|} \quad (4)$$

where  $RSCR_i$  means the self-centering ratio at the  $i$ th cycle,  $\theta_{\text{resi}}$  means the residual deformation at the  $i$ th cycle, as shown in Fig. 11(a).

The relative self-centering ratio-drift curves of all connections are shown in Fig. 13. The RSCRs of the six specimens exhibited decreasing trends when the drift exceeded 1%, owing to the cumulatively accumulated plastic deformation. The AMBC, as an assembled monolithic beam-to-column connection, typically had a relatively low self-centering ratio when the drift surpasses 1%. The condition of the

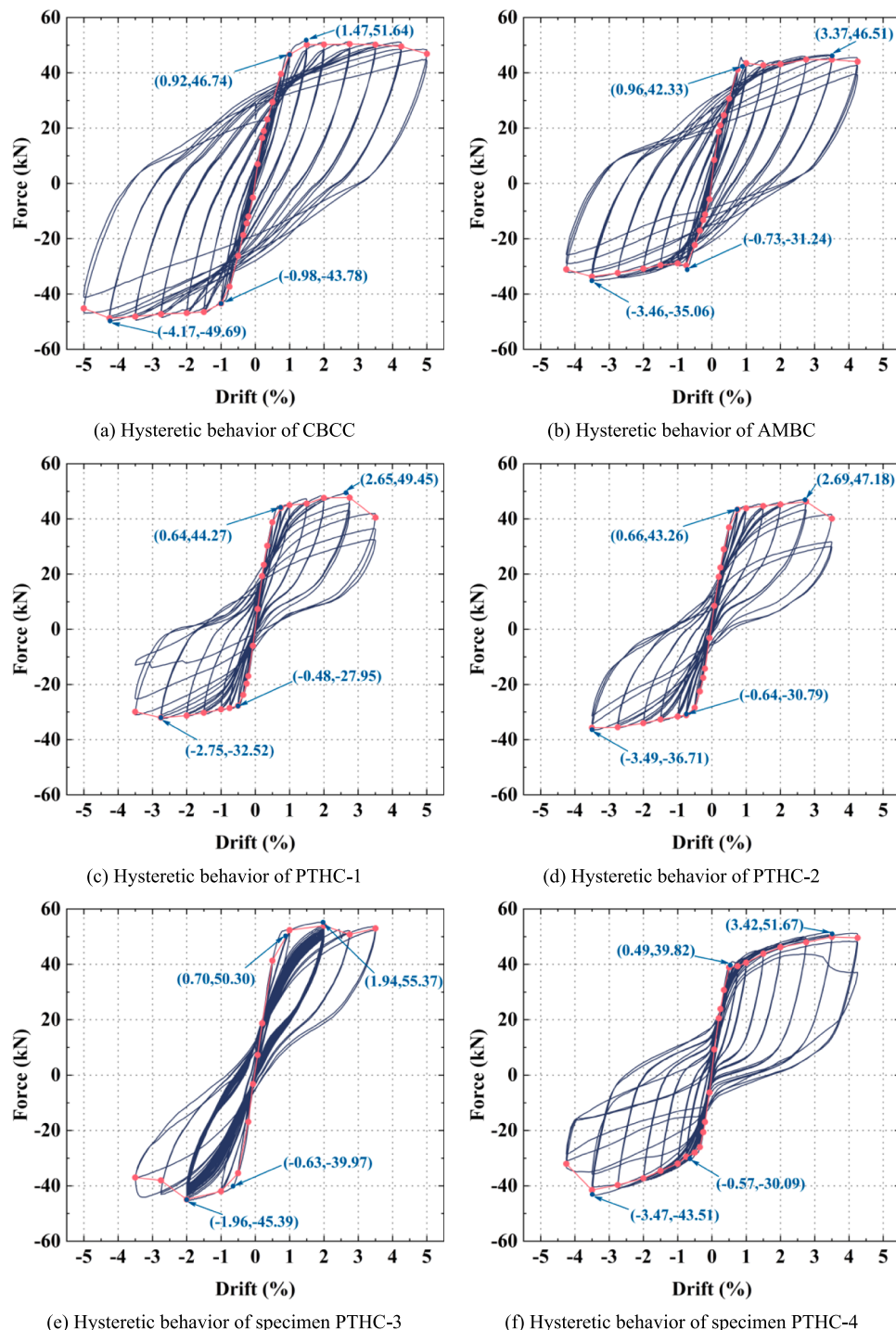


Fig. 8. Hysteresis curves of specimens.

AMBC was similar to that of the CBC, and the final self-centering ratio was 35.86%. In relative terms, the self-centering capabilities of the hybrid connections were much better than those of the AMBC and the CBC. Compared to the other three PTHC specimens, PTHC-3 showed an increase in the initial prestress force by approximately 64%; therefore, its self-centering ratio (85.86%) was significantly higher than that of the other hybrid connections. Considering that the mild steel strips contributed a large proportion of the section resistance moment when entered the plastic stage, PTHC-4 had a relatively weak recentering ability. As the plastic deformation of mild steel has increased, its contribution to the carrying capacity of the connection has increased

while the residual deformation has become larger. When the PTHC-4 loaded to 4.25% drift ratio, the mild steel in the lower part of the connection suddenly fractured and the residual deformation was released, resulting in a sudden increase in the self-centering rate of the connection at this drift. In general, the self-centering rate of PTHC-4 was lower than that of PTHC-1 and PTHC-2, partly due to the higher energy dissipation capacity of the mild steel, which generated more self-centering resistance, and partly due to less damage at the beam ends and greater actual gap opened.

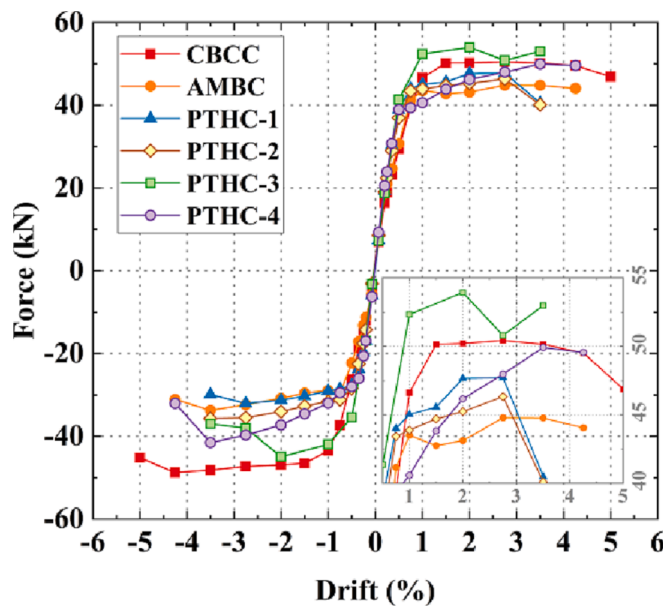


Fig. 9. Envelope curves of specimens.

### 3.7. Strain response

To determine the stress states of the hybrid connections under different deformations more accurately, strain gauges were attached to both the bars and energy-dissipating elements, which is shown in Fig. 5. The strain curves of the longitudinal and unbonded energy-dissipating bars in the prefabricated beams are shown in Fig. 14; the maximum strain of B-100-L1 was  $-364.74 \mu\epsilon$ , which was much lower than the nominal yield strain of the rebar. In contrast, when the drift reached 0.33%, the energy-dissipating bar of PTHC-1 first entered the plasticity state; subsequently, the unbonded bar exhibited remarkable plasticity when the specimen was loaded to a drift of 0.50%.

The relationship between the normalized time and the strain of an energy-dissipating element is shown in Fig. 15. The strains of the unbonded bars in PTHC-1 were significantly higher than of those in the other specimens, at the same drift. The unbonded length of PTHC-2 was longer than that of PTHC-1, and it entered the plasticity state at a drift of 0.75%, which was delayed compared to those of the other connections. The yield drifts of the energy-dissipating elements in PTHC-1 and PTHC-4 were almost simultaneous, and the yield phenomenon was observed at a 0.50% drift.

## 4. Numerical analysis

### 4.1. Comparison of experimental and numerical results

To further investigate the performance of PTHC connections, an FE

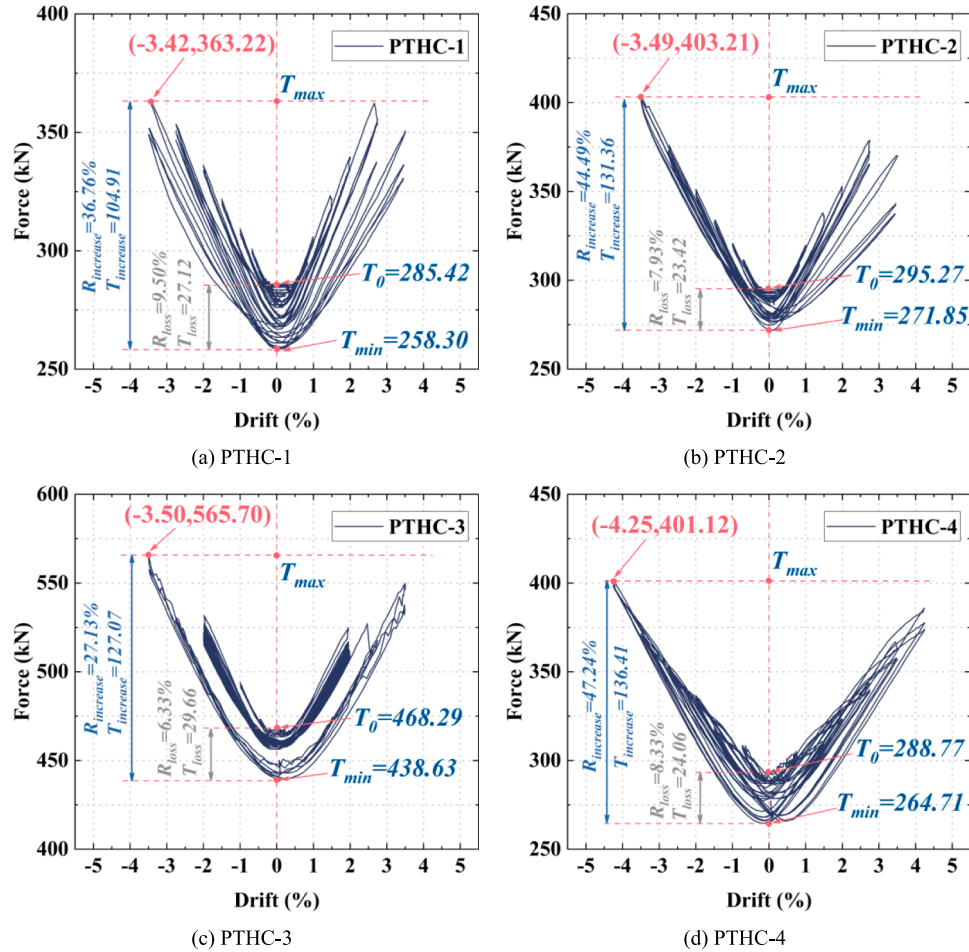


**Fig. 10.** Tension force versus drift response curves of PTHC specimens Notes:  $T_0$  is the initial prestress,  $T_{min}$  is the minimum prestress,  $T_{max}$  is the maximum prestress,  $T_{increase}$  is the growth value of prestress,  $R_{increase}$  is the growth rate of prestress,  $T_{loss}$  is the loss value of prestress,  $R_{loss}$  is the loss rate of prestress.

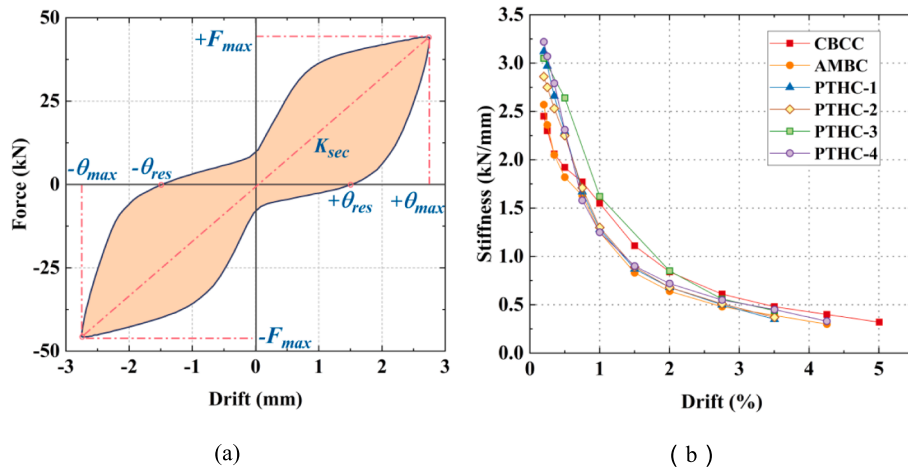


Fig. 11. Lateral stiffness of specimens.

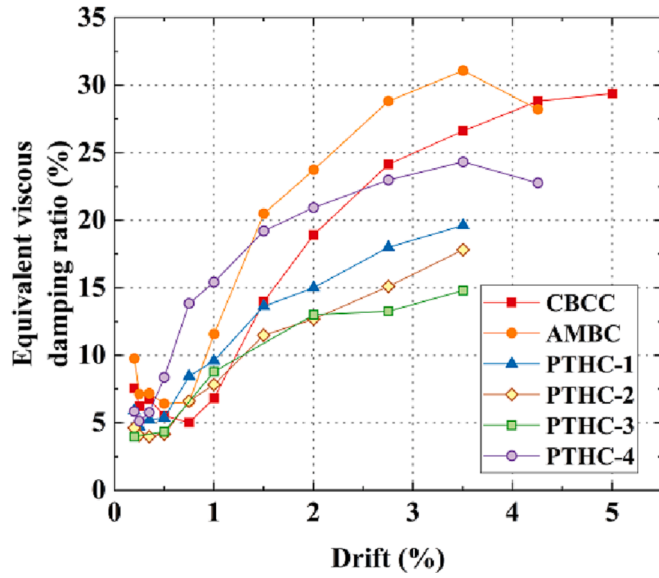


Fig. 12. Equivalent viscous damping coefficient curves of specimens.

model is established using ABAQUS, which is shown in Fig. 16. Each beam and column are simulated using C3D8R elements, and T3D2 elements [30] are applied to simulate the reinforcements, energy-dissipating elements, and PT strands. The approximate global size of mesh seed for beam and column was 40 mm and the bars was 20 mm. The bottom of the column was fully pinned, and only vertical displacement was restrained at the beam end. In order to make the numerical model more convergent, a viscosity parameter of 0.005 was introduced to the concrete to ensure the stability of the calculation. The interactions among the PT strands and the beam–column are established by multi-point constraints [28], and “temperature field via cooling tendons” is used to apply the prestress force. The concrete damage plastic model [42] is applied to each beam and column, and cyclic hardening constitution [43] is used to simulate the energy-dissipating elements.

The interaction between the beam and column of a specimen is simulated using contact pairs. The normal behavior is hard contact, and for the tangential behavior of the contact surfaces, the Coulomb-friction model is employed. The anchor areas of the energy-dissipating elements are embedded in the concrete, and no contact is established between the unbonded PT strands and the beam-to-column connections.

The numerical model is cycled using the same loading procedure

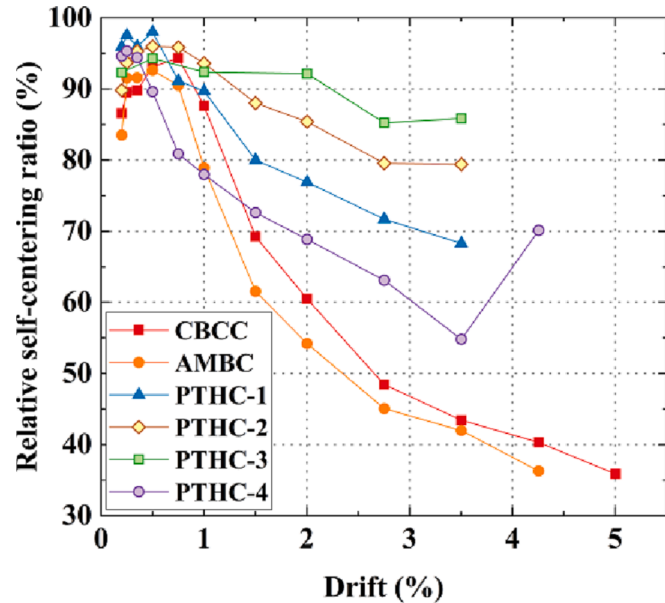


Fig. 13. Relative self-centering ratios of specimens.

used in the experiments. Fig. 17 compares the simulated hysteresis curves of the PTHC specimens with those from the test results. It can be seen that the shapes of the hysteresis curves obtained from the simulations are consistent with those from the experimental results. Moreover, the maximum bearing capacity obtained from the simulations is also in good agreement with the test results before the strength degradation.

#### 4.2. Parametric studies

The validity of the ABAQUS modeling method has been verified, and in view of the limited test data, further parametric analysis of the hybrid connections is conducted using the ABAQUS software. The model for the parametric analysis is based on PTHC-1, and the unbonded lengths, equivalent areas of the energy-dissipating elements, and initial prestress force of the specimen are varied to assess their effects. The specific parameters are listed in Table 4.

The prestressing tendons are the core components of the hybrid connections, which provide both flexural load capacity to the connections and shear load capacity to the beam–column interface by generating sufficient frictional forces by precompression.

Fig. 18(a) shows the hysteresis curves obtained using the analytical

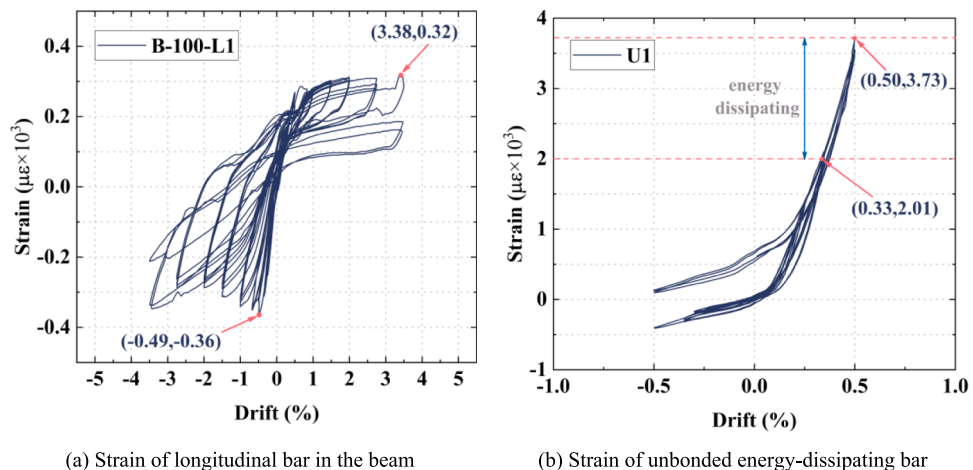


Fig. 14. Strain–drift ratio curves of PTHC-1.

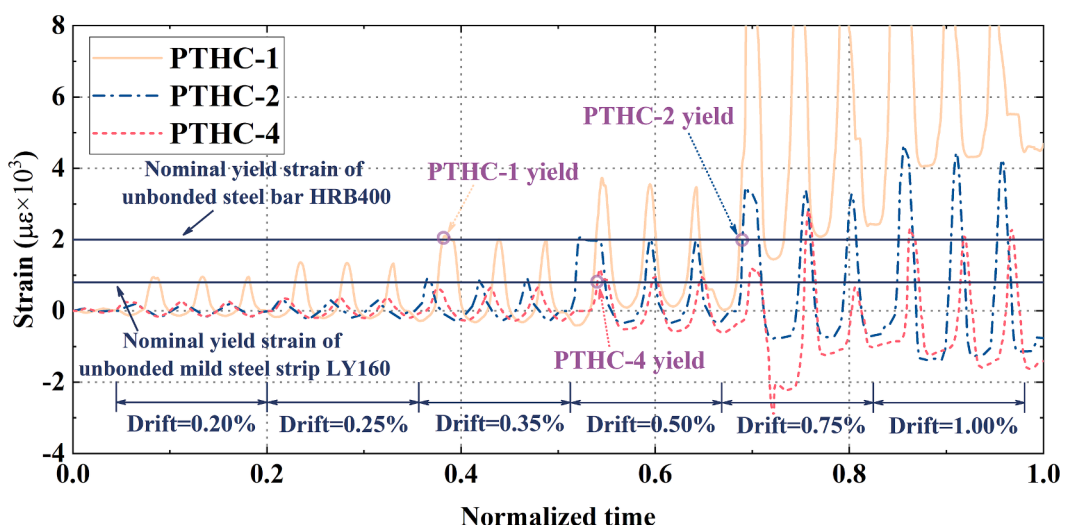


Fig. 15. Strain–normalized time curves of unbonded energy-dissipating elements.

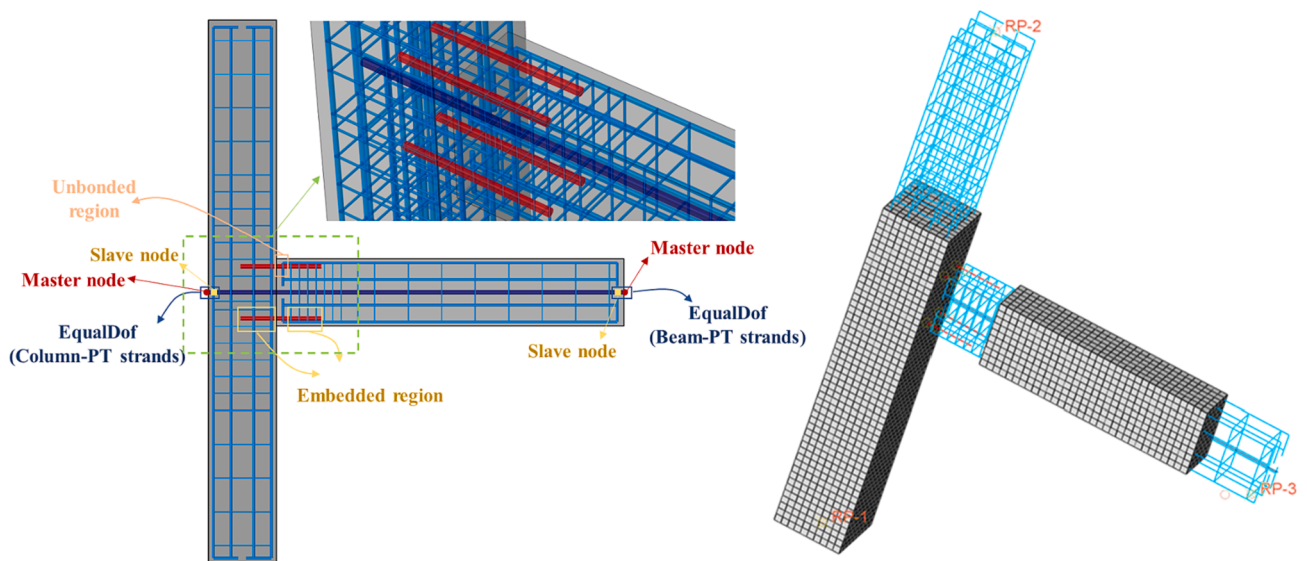
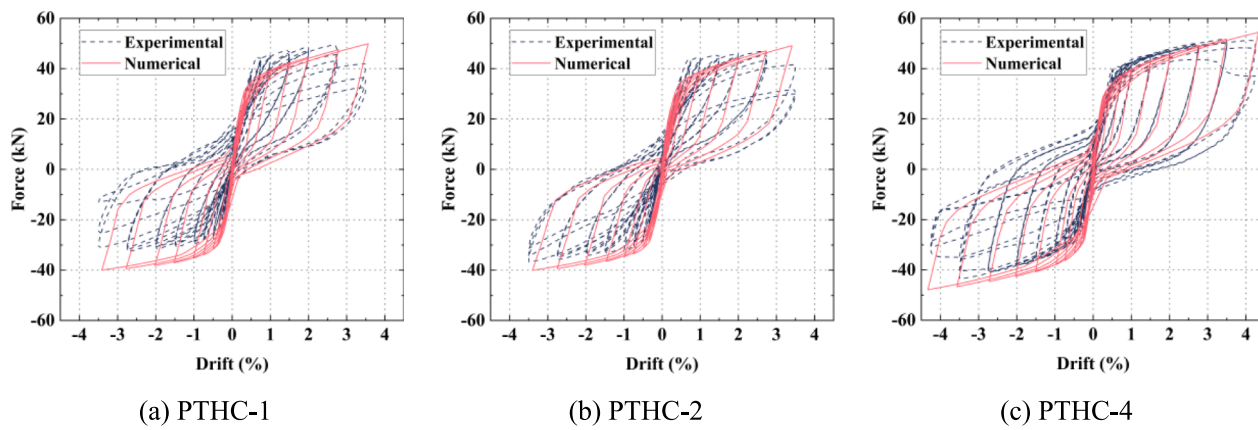


Fig. 16. FE model of PTHC specimens.



**Fig. 17.** Comparison of hysteretic behavior obtained from analytical and experimental results.

**Table 4**  
Parameters for analysis.

Specimen	Unbonded length	Equivalent areas of Energy-dissipating elements	Initial prestress force
PTHC-L40	40 mm	1.0A	0.27 Tu
PTHC-L60	60 mm	1.0A	0.27 Tu
PTHC-L120	120 mm	1.0A	0.27 Tu
PTHC-L200	200 mm	1.0A	0.27 Tu
PTHC-L300	300 mm	1.0A	0.27 Tu
PTHC-1.0A	60 mm	1.0A	0.27 Tu
PTHC-1.5A	60 mm	1.5A	0.27 Tu
PTHC-2.0A	60 mm	2.0A	0.27 Tu
PTHC-2.5A	60 mm	2.5A	0.27 Tu
PTHC-3.0A	60 mm	3.0A	0.27 Tu
PTHC-0.27Tu	60 mm	1.0A	0.27 Tu
PTHC-0.35Tu	60 mm	1.0A	0.35 Tu
PTHC-0.45Tu	60 mm	1.0A	0.45 Tu
PTHC-0.60Tu	60 mm	1.0A	0.60 Tu
PTHC-0.75Tu	60 mm	1.0A	0.75 Tu

model, where the load capacity of the connections is observed to increase as the initial prestress increases. The initial prestress and maximum load capacity of PTHC-0.60Tu increase by 122.22% and 34.08%, respectively, compared to those of PTHC-0.27Tu. The PT strands have no apparent yield point, and their conditional yield

strength is set at 0.85 times the ultimate tensile strength. The initial prestress force of PTHC-0.75Tu is 781.20 kN, which increases to 940.91 kN at a drift of 3.50%, which is close to the yield strength value of 963.20 kN, as shown in Fig. 18(b). From the above analysis, it can be concluded that increasing the initial prestressing force can effectively improve the maximum bearing and self-centering capacity of the connections. To ensure that the PT strands are in an elastic state, the initial prestressing must be reasonably designed and should not exceed 0.75 times the ultimate strength. The equivalent viscous damping ratios corresponding to the maximum displacements of these five specimens are 17.52%, 15.95%, 14.71%, 12.62%, and 11.06% respectively, showing a gradual decrease trend.

The load-carrying capacity values of the hybrid connections are increased by both the PT strands and unbonded energy-dissipating elements. Specifically, the equivalent areas of the latter considerably affect the load-carrying capacity and energy dissipation of the hybrid connections. As shown in Fig. 19(a), the envelope area of the hysteresis curve increases as the equivalent areas of the energy-dissipating elements increase, and the residual deformation accumulates. The maximum bearing capacity values of the five numerical models are 52.92 kN, 60.07 kN, 68.16 kN, 76.27 kN, and 84.78 kN, respectively. The equivalent areas of the energy-dissipating bars have a significant effect on the load capacity of the PTHC specimens, as shown in Fig. 19(b). The hysteresis curves of the energy-dissipating bars and the equivalent viscous damping ratios from the numerical models are shown in Fig. 19(c) and (d).

The maximum equivalent viscous damping ratios of the five models are 17.52%, 21.71%, 24.60%, 26.75%, and 27.77%, respectively. By

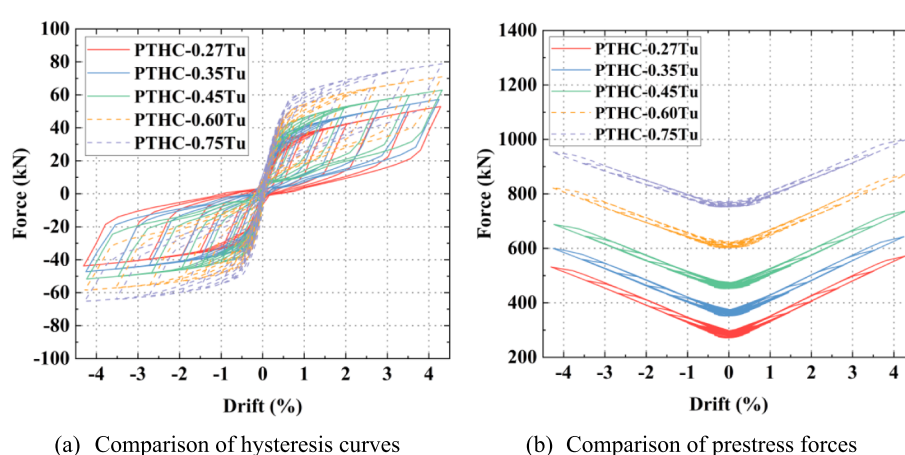


**Fig. 18.** Parametric analysis of initial prestress.

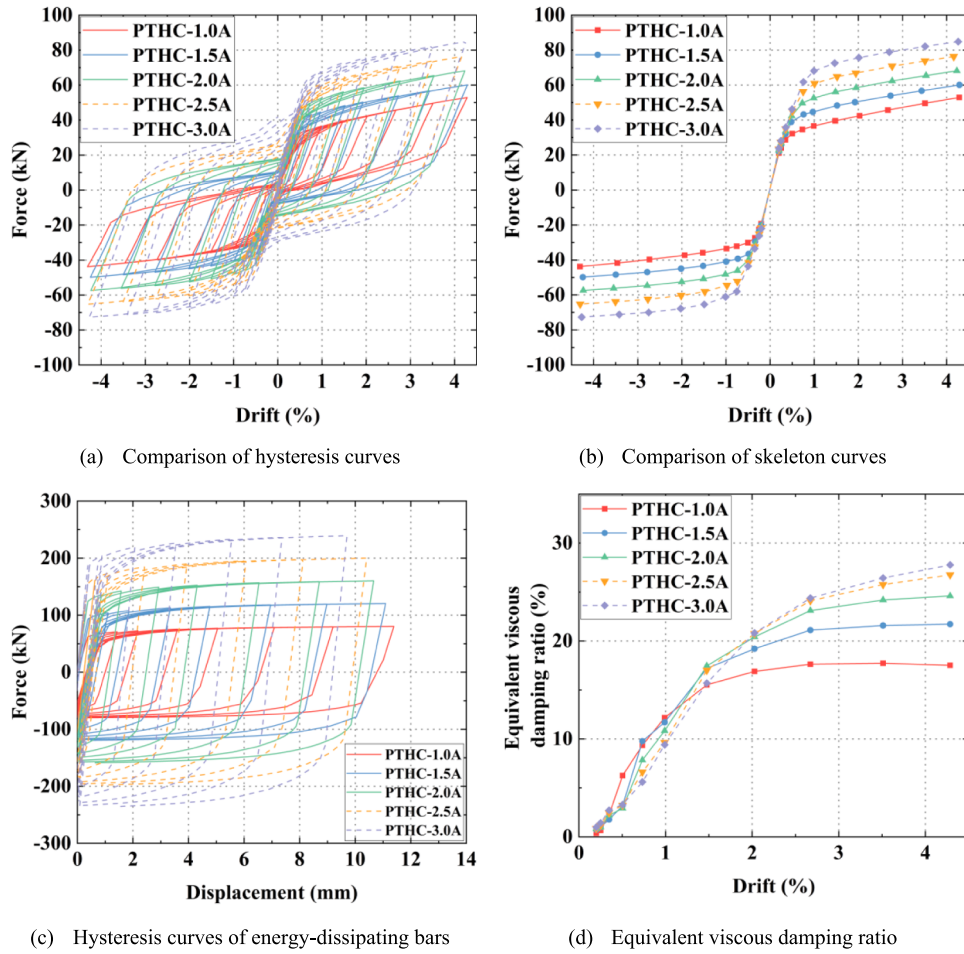


Fig. 19. Parametric analysis of the equivalent area.

increasing the equivalent areas of the energy-dissipating bars, the load capacity and energy dissipation of the hybrid connections can be effectively increased. Concurrently, a certain proportion of the self-centering capacity will be sacrificed. Therefore, the design of PTHC systems must balance the PT force and the energy-dissipating areas.

To further investigate the effect of the unbonded length, all parameters except the lengths of the energy-dissipating elements in the five numerical models are controlled, and the results are shown in Fig. 20. The maximum equivalent viscous damping ratios of the five models are

18.91%, 18.80%, 17.52%, 16.46%, and 15.07%, respectively. When the unbonded length is long, the yield drift is high, the ultimate force is small, and the energy dissipation is relatively weak, as shown in Fig. 20 (b). The main energy dissipation mechanism of the hybrid connections is the hysteresis energy dissipation of the unbonded parts. Thus, the energy dissipation behavior of the connections is consistent with the behavioral pattern of the energy-dissipating bars. In general, under the premise of satisfying the fatigue performance, shorter design lengths of the energy-dissipating elements will be more conducive to the seismic performance

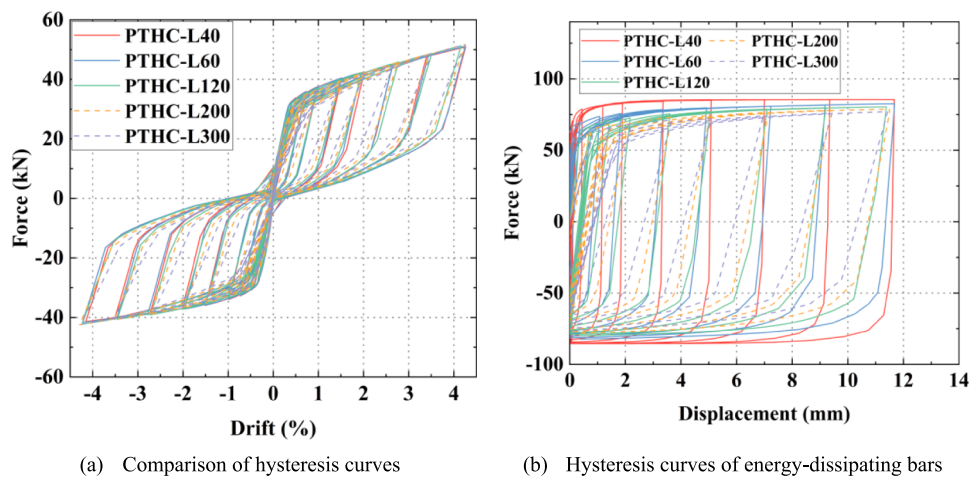


Fig. 20. Parametric analysis of unbonded length.

of PTHC systems.

## 5. Conclusions

This study developed novel self-centering PTHCs. The design parameters of the unbonded length, material of the energy-dissipating elements, initial prestress, and beam-end constraint construction measures were investigated. Numerical modeling was performed using ABAQUS, and further numerical studies were conducted on the design parameters. The main conclusions of this study were as follows.

(1) Angle steel with anchorage measures positioned at the beam end can protect the beam-end concrete and effectively restrain the buckling of the unbonded energy-dissipating elements. PTHC-4 has a delayed initial crack appearance and lesser concrete damage than PTHC-1 and PTHC-2, which do not have constrained configurations. A suitable beam-end restraint construction measure can effectively transfer the internal forces of the energy-dissipating elements and ensure their efficient energy dissipation.

(2) The PTHC systems present good seismic performance and strong energy dissipation capacity. The components have low damage, good self-centering capacity, easy repairability, and satisfy the fatigue performance requirements up to a 2% drift ratio. PTHC-3 and PTHC-4 do not show a considerable reduction in the load-carrying capacity at a 3.5% drift ratio, suggestive of good collapse resistance capacity in response to an unanticipated earthquake. The PTHC specimens present much smaller residual deformation, similar load capacity, and superior seismic toughness than the CBCC and the AMBC.

(3) The lengths of the unbonded energy-dissipating elements have almost no effect on the yield and ultimate forces of the PTHC specimens. However, based on the FE analysis, it has a considerable influence on the energy dissipation capacity. The PTHC specimens with shorter unbonded energy-dissipating lengths have smaller yield displacement, greater initial stiffness, and higher energy-dissipation capacity, but smaller ultimate deformation and lower self-centering capacity. Therefore, on the premise of meeting the target deformation capacity and fatigue performance, it is recommended to adopt shorter unbonded length of energy dissipating bars.

(4) Increasing the initial prestressing force can effectively increase the maximum load capacity and the self-centering ratio of the PTHC specimens, whereas it has virtually no improvement on the energy dissipation efficiency. The loss rates of the prestress during reciprocating loading are between 6% and 10%, and the growth rates are less than 50%; moreover, none of the PT strands yield and the stresses are within safe limits. The self-centering rates of the PTHC specimens are above 50%, and the residual deformation is reduced by at least 57.14% compared to those of conventional connections. Combining with the results of the FE analysis, it's suggested that to ensure that the PT strands are in an elastic state, the initial prestress should not exceed 0.75 times the ultimate strength of the PT strands.

(5) The detailed FE model is sufficiently accurate in predicting the behavior of the PTHC specimens, and the parametric numerical simulations show that the equivalent areas of the energy-dissipating elements considerably affect the load-carrying capacity and energy dissipation of the hybrid connections. As the energy-dissipating area increases from 452.16 mm<sup>2</sup> to 1356.48 mm<sup>2</sup>, the maximum load capacity of the connection rises by 60.20% and the equivalent viscous damping ratio increases by 58.50%, whereas the residual deformation accumulates with the increase of equivalent areas. Therefore, balancing the equivalent energy-dissipating areas and the initial prestress is key to the design of a PTHC system.

It should be noted that the proposed novel self-centering PTHCs are simpler construct design and convenient to construct. However, the built-in energy-dissipating elements means that the connections are prone to loss of energy dissipation capacity after earthquake damage. Therefore, for the post-earthquake repair work of PTHCs and the functional recovery capacity still need further study.

## Declaration of Competing Interest

The authors declare that they have no known competing financial interests or personal relationships that could have appeared to influence the work reported in this paper.

## Acknowledgments

The authors are greatly thankful for the Scientific Research Fund of Multi-Functional Shaking Tables Laboratory of Beijing University of Civil Engineering and Architecture (2022MFSTL03) and National Natural Science Foundation of China (52208173). The authors are also grateful for the support received from the Fellowship of China Postdoctoral Science Foundation (2022M721591).

## References

- [1] Fan J-J, Wu G, Feng D-C, Zeng Y-H, Lu Y. Seismic performance of a novel self-sustaining beam-column connection for precast concrete moment-resisting frames. Eng Struct 2020;222:111096.
- [2] Ghayeb HH, Abdul Razak H, Ramli Sulong NH. Seismic performance of innovative hybrid precast reinforced concrete beam-to-column connections. Eng Struct 2020; 202:109886.
- [3] Ghayeb HH, Razak HA, Sulong NHR. Development and testing of hybrid precast concrete beam-to-column connections under cyclic loading. Constr Build Mater 2017;151:258–78.
- [4] Gou SK, Ding R, Fan JS, Nie X, Zhang J. Seismic performance of a novel precast concrete beam-column connection using low-shrinkage engineered cementitious composites. Constr Build Mater 2018;192:643–56.
- [5] Xue WC, Hu XY, Dai LJ, Zhu B. Cyclic behavior of semi-rigid precast concrete beam-to-column subassemblages with rapid assembly connections. J Build Eng 2022;46:103671.
- [6] Parastesh H, Hajirasouliha I, Ramezani R. A new ductile moment-resisting connection for precast concrete frames in seismic regions: An experimental investigation. Eng Struct 2014;70:144–57.
- [7] Gu X-L, Zhang B, Huang X-K, Wang X-L. Experimental investigation on progressive collapse resistance of precast concrete frame structures with different beam-column connections. J Build Eng 2022;56:104803.
- [8] Huang W, Hu G, Miao X, Fan Z. Seismic performance analysis of a novel demountable precast concrete beam-column connection with multi-slit devices. J Build Eng 2021;44:102663.
- [9] Wang CL, Liu Y, Zheng X, Wu J. Experimental investigation of a precast concrete connection with all-steel bamboo-shaped energy dissipaters. Eng Struct 2019;178: 298–308.
- [10] Li YD, Geng FF, Ding YL, Wang LB. Influence of mild steel damper design parameters on energy dissipation performance of low-damage self-centering precast concrete frame connections. Soil Dynam Earthq Eng 2021;144:106696.
- [11] Cai XN, Pan ZF, Zhu YZ, Gong NN, Wang YW. Experimental and numerical investigations of self-centering post-tensioned precast beam-to-column connections with steel top and seat angles. Eng Struct 2021;226:111397.
- [12] Park R. Seismic design and construction of precast concrete buildings in New Zealand. PCI J 2002;47(5):60–75.
- [13] Huang LJ, Clayton PM, Zhou Z. Seismic design and performance of self-centering precast concrete frames with variable friction dampers. Eng Struct 2021;245: 112863.
- [14] Priestley MJN. Overview of PRESSS research program. PCI J 1991;36(4):50–7.
- [15] Stanton J, Stone WC, Cheek GS. A hybrid reinforced precast frame for seismic regions. PCI J 1997;42(2):20–3.
- [16] Stone WC, Cheek GS, Stanton JF. Performance of hybrid moment-resisting precast beam-column concrete connections subjected to cyclic loading. ACI Struct J 1995; 92(2):229–49.
- [17] Morgen BG, Kurama YC. A friction damper for post-tensioned precast concrete moment frames. PCI J 2004;49(4):112–33.
- [18] Morgen BG, Kurama YC. Seismic design of friction-damped precast concrete frame structures. J Struct Eng 2007;133(11):1501–11.
- [19] Koshikawa T. Moment and energy dissipation capacities of post-tensioned precast concrete connections employing a friction device. Eng Struct 2017;138:170–80.
- [20] Li YD, Geng FF, Ding YL, Wang LB. Experimental and numerical study of low-damage self-centering precast concrete frame connections with replaceable dampers. Eng Struct 2020;220:111011.
- [21] Geng FF, Ding YL, Wu HL, Yang JP, Shen W. Seismic performance enhancing of novel self-centering precast concrete frame using replaceable hysteretic dampers. J Build Eng 2021;42:103059.
- [22] Liu Y, Wang WY. Concept and analysis of a low-cost energy dissipater with partially self-centering mechanism. J Build Eng 2021;44:102881.
- [23] Bai JL, He J, Li C, Jin SS, Yang H. An RBS-based replaceable precast concrete beam-column joint: Design approach and experimental investigation. J Build Eng 2022; 51:104212.
- [24] Lu Z, Huang J, Dai S, Liu J, Zhang M. Experimental study on a precast beam-column joint with double grouted splice sleeves. Eng Struct 2019;199:109589.

- [25] Ozden S, Ertas O. Behavior of unbonded, post-tensioned precast concrete connections with different percentages of mild steel reinforcement. *PCI J* 2007;52(2):32–44.
- [26] Song GE, Yang TY, Zhou Y. Distribution of hysteretic energy demands in self-centering concrete frames with hybrid joints. *Soil Dynam Earthq Eng* 2021;148:106828.
- [27] Wang HS, Marino EM, Pan P, Liu H, Nie X. Experimental study of a novel precast prestressed reinforced concrete beam-to-column joint. *Eng Struct* 2018;156:68–81.
- [28] Wang HS, Marino EM, Pan P. Design, testing and finite element analysis of an improved precast prestressed beam-to-column joint. *Eng Struct* 2019;199:109661.
- [29] Wang HS, Barbagallo F, Pan P. Test of precast pre-stressed beam-to-column joint with damage-free reinforced concrete slab. *Eng Struct* 2020;210:110368.
- [30] Li DB, Chai YK, Li WL, Xiang R. Experimental study and finite element analysis of seismic behaviour of novel precast prestressed concrete frames. *Struct* 2022;38:402–15.
- [31] Song BX, Xu WZ, Du DS, Wang SG, Li WW, Zhang YL. Seismic design of hybrid unbonded post-tensioned precast concrete joints based on bearing capacity and energy dissipation capacity. *Adv Struct Eng* 2020;24(1):1724–38.
- [32] Song BX, Xu WZ, Du DS, Wang SG. Quantification of moment-rotation relationship of monolithic precast beam-column connections. *Buildings* 2021;12(1):11.
- [33] GB 50010-2010. Code for design of concrete structures. Beijing: China Building Industry Press; 2010. (In Chinese).
- [34] Xu WZ. Research on the Synergistic Damping Structure System and Seismic Performance of Post-tensioned precast Concrete Frame. Nanjing Tech University; 2021. Ph.D. Dissertation.
- [35] GB/T 50107-2010. Standard for evaluation of concrete compressive strength. Beijing: China Building Industry Press; 2010. (In Chinese).
- [36] GB 50011-2010.. Code for seismic design of buildings. Beijing: China Building Industry Press; 2010. In Chinese.
- [37] JGJ 297-2013.. Technical specification for seismic energy dissipation of buildings. Beijing: China Building Industry Press; 2013. In Chinese.
- [38] Feng P, Cheng S, Bai Y, Ye L. Mechanical behavior of concrete-filled square steel tube with FRP-confined concrete core subjected to axial compression. *Compos Struct* 2015;123:312–24.
- [39] Lu C, Dong B, Pan J, Shan Q, Hanif A, Yin W. An investigation on the behavior of a new connection for precast structures under reverse cyclic loading. *Eng Struct* 2018;169:131–40.
- [40] Xue W, Huang Q, Li Y. Experimental study of precast concrete shear walls with spiral-confined lap connections under cyclic loads. *J Build Eng* 2022;52:104467.
- [41] Hu X, Xue W, Zhang B. Cyclic response of concrete frame with precast column and U-shaped composite beam. *Struct* 2022;43:465–78.
- [42] Xue W, Hu X, Song J. Experimental study on seismic behavior of precast concrete beam-column joints using UHPC-based connections. *Struct* 2021;34:4867–81.
- [43] Rahmzadeh A, Iqbal A. Numerical modelling and analysis of post-tensioned timber beam-column joint. *Engineering Struct* 2021;245:112762.